



Article

Fluorinated Tolane Dyads with Alkylene Linkage: Synthesis and Evaluation of Photophysical Characteristics

Shigeyuki Yamada ^{1,*} , Eiji Uto ¹, Tomohiro Agou ² , Toshio Kubota ² and Tsutomu Konno ¹¹ Faculty of Molecular Chemistry and Engineering, Kyoto Institute of Technology, Matsugasaki, Sakyo-ku, Kyoto 606-8585, Japan; kit.fusso.201901@gmail.com (E.U.); konno@kit.ac.jp (T.K.)² Department of Quantum Beam Science, Graduate School of Science and Engineering, Ibaraki University, 4-12-1 Naka-narusawa, Hitachi, Ibaraki 316-8511, Japan; tomohiro.agou.mountain@vc.ibaraki.ac.jp (T.A.); toshio.kubota.organicchem@vc.ibaraki.ac.jp (T.K.)

* Correspondence: syamada@kit.ac.jp; Tel.: +81-75-724-7517

Received: 20 July 2020; Accepted: 16 August 2020; Published: 18 August 2020



Abstract: Light-emitting materials have received considerable attention because of their broad applications as substrates in bio-imaging and sensing components, light-emitting displays, and lighting devices. Herein, we developed fluorinated tolane and bistolane derivatives containing fluorinated aromatic rings and demonstrated their intense photoluminescence (PL) characteristics in crystalline powder states. We focused on molecules showing varied PL behavior with a change in the molecular aggregated structures. We synthesized novel fluorinated tolane dyads consisting of fluorinated tolane-based π -conjugated scaffolds and flexible alkylene linkages to control both the electron-density distribution and molecular aggregated states. Fluorinated tolane dyads connected with an alkylene linkage showed blue PL in a dilute solution, but the PL efficiency achieved was low. In contrast, the crystalline powder of tolane dyad substrates exhibited dual emission—relatively intense blue to deep blue PL—originating from monomer and aggregate emission. The PL behavior changed significantly with the alkylene linkage and the application of a mechanical stimulus to the crystalline powder sample. The fluorinated tolane dyads developed in this study could serve as stimulus-responsive photoluminescent materials suitable for optical applications.

Keywords: fluorinated tolane; dyads; photoluminescence; mechanical stress; stimulus-responsive molecules

1. Introduction

In the past few decades, significant advancements have been realized for light-emitting materials, and many such materials have been utilized in practical contexts [1–3]. They are generally classified as solution or solid-state light-emitting materials. The former exhibits luminescence in the solution state and usually consists of an extended π -conjugated structure. Examples include pyrene and perylene, which serve as bio-imaging or sensing probes [4–6]. Solid-state light-emitting materials show luminescence in solid states and are mainly applicable to light-emitting displays or lighting devices [7–10]. It has been challenging to develop solid-state light-emitting molecules due to the luminescence quenching effect induced by the formation of molecular aggregates [11]. Since epoch-making reports have been published by Tang and coworkers, the exploration of novel solid-state light-emitting molecules has accelerated and several molecular designs to suppress non-radiative deactivation processes in the molecular aggregated states have been proposed [12–15]. In addition to significant advances being made in the field of solid-state light-emitting molecules, it has been increasingly noted that many unique luminescence materials show a change in the

luminescence color or intensity when an external stimulus is applied. These have therefore been named stimulus-responsive photoluminescent molecules [16–21]. In spite of their wide utility, progress in terms of the molecular design of solid-state photoluminescent molecules has been quite limited; accordingly, the search for efficient solid-state photoluminescent molecules is still on.

Since a few years ago, we have extensively developed solid-state photoluminescent molecules based on the extended π -conjugated structure containing a fluorinated aromatic structure, which induces electron-density distribution owing to its large electronegativity and forms a tight crystal structure via van der Waals and hydrogen bonding interactions [22–28]. Among them, polyfluorinated tolane **1a** [27] displayed highly efficient blue photoluminescence (PL) ($\Phi_{\text{PL}} = 0.73$) in crystalline states, although the PL efficiency was observed to be significantly low in dilute solution ($\Phi_{\text{PL}} = \sim 0.04$) (Figure 1a). With deep investigations, interestingly, the PL behavior of **1a** and the non-fluorinated analogue on the aromatic ring was found to change with an alteration of the molecular aggregated structures in the crystalline lattice; it was shown that fluorine atoms attached to an aromatic ring offering control over the molecular aggregated structure and photophysical behavior.

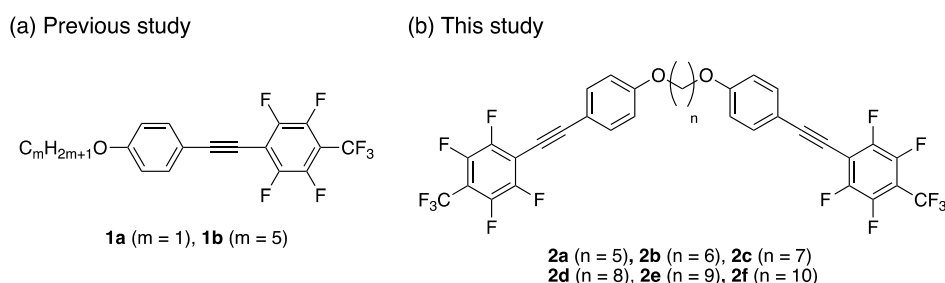


Figure 1. (a) Solid-state photoluminescent molecules **1** containing fluorinated aromatic structures developed in our group and (b) molecular structure for new solid-state photoluminescent molecules **2** designed in this study.

Based on the knowledge we acquired on the photophysical behavior of such fluorinated π -conjugated molecules, e.g., **1a**, we envisioned that dyads **2a–f** consisting of two fluorinated tolane-based luminophore **1a** and an alkyne linkage as a spacer could take up a different molecular geometry depending on the linkage length, based on factors such as the odd–even effect [29–32]. Therefore, we constructed various molecular aggregated structures to display various photophysical behaviors. Herein, we disclose the theoretical design of molecular structures, synthesis of the new fluorinated tolane dyads **2a–f**, and their photophysical characteristics in detail. Additionally, the mechanochromic PL behavior of **2** upon mechanical stress in mortar is also demonstrated.

2. Materials and Methods

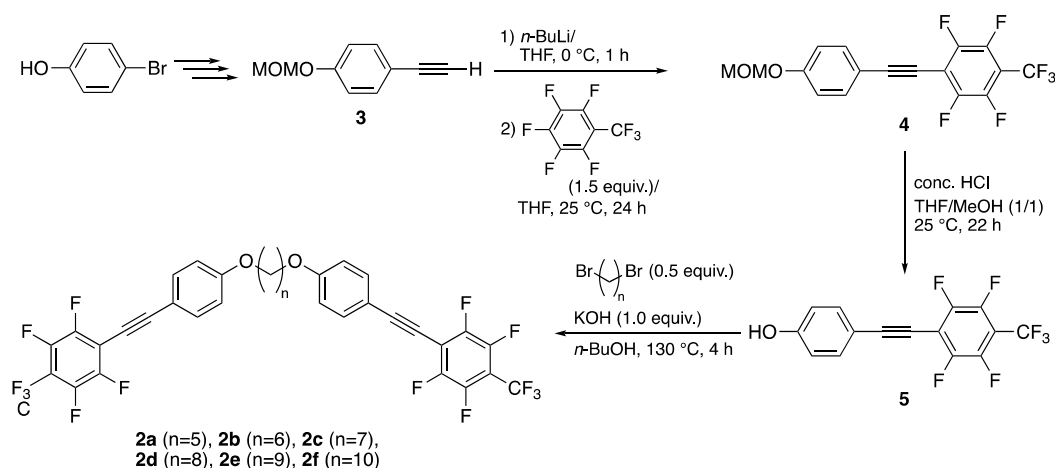
2.1. General

Infrared (IR) spectra were acquired using KBr pellets containing the samples employing an FT/IR-4100 type A spectrometer (JASCO, Tokyo, Japan); all spectra are reported in wavenumber (cm^{-1}) units. ^1H (400 MHz) and ^{13}C -nuclear magnetic resonance (NMR) (100 MHz) spectra were recorded on an AVANCE III 400 NMR spectrometer (Bruker, Rheinstetten, Germany) in chloroform- d (CDCl_3) solution. The chemical shifts are reported in parts per million (ppm) against the residual proton in the NMR solvent. ^{19}F NMR (376 MHz) spectra were acquired using an AVANCE III 400 NMR spectrometer (Bruker, Rheinstetten, Germany) in CDCl_3 solution with CFCl_3 ($\delta_{\text{F}} = 0$ ppm) as an internal standard. High-resolution mass spectroscopy (HRMS) was taken on a JMS-700MS spectrometer (JEOL, Tokyo, Japan) by fast atom bombardment (FAB). All reactions were carried out under an atmosphere of argon using dried glassware with a magnetic stir bar. All chemicals were of reagent grade and were purified in the usual manner prior to use when necessary. Column chromatography was conducted using silica gel (FUJIFILM Wako Pure Chemical Corporation, Wakogel® 60N, 38–100 μm ; Osaka, Japan) and

thin layer chromatography (TLC) was performed on silica gel TLC plates (Merck, Silica gel 60F₂₅₄; Kenilworth, NJ, USA).

2.2. Materials

The fluorinated tolane dyads **2a–f** connected with an alkylene spacer used in this study were prepared in a facile three-step procedure from 4-(methoxymethoxy)phenylacetylene **3**, which was readily available from commercially available 4-bromophenol, as shown in Scheme 1.



Scheme 1. Synthetic route for the fluorinated tolane dyads **2a–f**.

2.3. Preparation of 1-Trifluoromethyl-2,3,5,6-tetrafluoro-4-[2-(4-methoxymethoxyphenyl)ethyn-1-yl]benzene (**4**) via an Addition–Elimination Process

In a 50 mL flask, 4-(methoxymethoxy)phenylacetylene (**3**, 1.27 g, 7.8 mmol), which was prepared in three steps from commercially available 4-bromophenol according to a reported procedure [33–35], and tetrahydrofuran (THF, 78 mL) were introduced. To the solution, 1.6 mol L^{−1} hexane solution of *n*-butyllithium (7.2 mL, 11.5 mmol) was added dropwise at 0 °C and the solution was stirred at this temperature for 1 h. To the solution, octafluorotoluene (2.74 g, 11.6 mmol) was added slowly at 0 °C and the resulting solution was stirred at 25 °C for 24 h. The reaction mixture was poured into a saturated aqueous solution of ammonium chloride (NH₄Cl, 100 mL). The organic product was extracted using ethyl acetate (EtOAc, 100 mL, three times), and washed once with brine (200 mL). The collected organic layer was dried over anhydrous sodium sulfate (Na₂SO₄) and concentrated under reduced pressure using a rotary evaporator after removing the inorganic drying agent. The product was purified by silica-gel column chromatography using hexane/EtOAc (20/1) as an eluent to provide the title compound (**4**, 2.42 g, 6.4 mmol) in 82% yield as a white solid.

1-Trifluoromethyl-2,3,5,6-tetrafluoro-4-[2-(4-methoxymethoxyphenyl)ethyn-1-yl]benzene (**4**)

Yield: 82% (white solid); M.P.: 84.6–85.5 °C; ¹H NMR (CDCl₃): δ 3.49 (s, 3H), 5.22 (s, 2H), 7.06 (d, *J* = 8.8 Hz, 2H), 7.54 (d, *J* = 8.8 Hz, 2H); ¹³C NMR (CDCl₃): δ 56.2, 72.6 (t, *J* = 3.6 Hz), 94.2, 105.2 (q, *J* = 3.7 Hz), 108.8 (q, *J* = 34.4 Hz), 109.4 (t, *J* = 19.1 Hz), 114.1, 116.4, 120.8 (q, *J* = 275.1 Hz), 133.8, 144.1 (dm, *J* = 261.1 Hz), 146.7 (dm, *J* = 257.5 Hz), 158.8; ¹⁹F NMR (CDCl₃): δ −56.63 (t, *J* = 21.8 Hz, 3F), −135.4 to −135.7 (m, 2F), −141.4 to −141.9 (m, 2F); IR (KBr): ν 3020, 2970, 2944, 2228, 1649, 1520, 1493, 1345, 1274, 1173, 1152, 1081, 986, 839 cm^{−1}; HRMS (FAB⁺) *m/z* [M]⁺ calcd for C₁₇H₉F₇O₂: 378.0491; found: 378.0483.

2.4. Preparation of 4-(2-(2,3,5,6-Tetrafluoro-4-trifluoromethyl)phenylethyn-1-yl)phenol (**5**)

In a 100 mL flask, freshly prepared **4** (2.42 g, 6.4 mmol) in methanol (35 mL) and THF (32 mL) were introduced. To the solution, concentrated hydrochloric acid (12 N, 8.0 mL) was added dropwise

at 0 °C, and the mixture was stirred at 25 °C for 22 h. After stirring for 22 h, the volatile organic solvent was removed under reduced pressure and the residue was poured into H₂O (50 mL). The product was extracted with dichloromethane (CH₂Cl₂, three times), and the organic layer combined was washed with a saturated aqueous solution of sodium hydrogen carbonate (NaHCO₃, 50 mL), followed by brine (50 mL). The organic layer was dried over anhydrous Na₂SO₄, filtered, and evaporated under reduced pressure using a rotary evaporator. The residue was subjected to silica-gel column chromatography using hexane/EtOAc (10/1) as an eluent, giving rise to the title product **5** (1.84 g, 5.49 mmol) in 86% yield as a white solid.

4-(2-(2,3,5,6-Tetrafluoro-4-trifluoromethyl)phenylethyn-1-yl)phenol (**5**)

Yield: 86% (white solid); M.P.: 146.8–148.1 °C; ¹H NMR (CDCl₃): δ 5.11 (s, 1H), 6.86 (d, *J* = 8.8 Hz, 2H), 7.51 (d, *J* = 8.8 Hz, 2H); ¹³C NMR (CDCl₃): δ 72.5 (t, *J* = 4.3 Hz), 105.1 (t, *J* = 3.6 Hz), 108.8 (q, *J* = 35.2 Hz), 109.4 (t, *J* = 18.4 Hz), 113.4, 115.8, 120.8 (q, *J* = 275.0 Hz), 134.1, 142.6–145.5 (dm, *J* = 264.0 Hz), 145.2–148.3 (dm, *J* = 253.8 Hz), 157.2; ¹⁹F NMR (CDCl₃): δ −56.63 (t, *J* = 21.8 Hz, 3F), −135.5 to −135.8 (m, 2F), −141.4 to −141.9 (m, 2F); IR (KBr): ν 3413, 3047, 3019, 2224, 1659, 1589, 1494, 1347, 1281, 1238, 1170, 1102, 986, 836 cm^{−1}; HRMS (FAB⁺) *m/z* [M]⁺ calcd for C₁₅H₅F₇O: 334.0229; found: 334.0221.

2.5. Typical Procedure for Preparation of 1,5-Bis[4-{2-(2,3,5,6-tetrafluoro-4-(trifluoromethyl)phenyl)ethyn-1-yl}phenoxy]pentane (**2a**)

In a 50 mL flask, 1,5-dibromopentane (0.102 g, 0.44 mmol), 4-(2-(2,3,5,6-tetrafluoro-4-trifluoromethyl)phenylethyn-1-yl)phenol (**5**, 0.34 g, 1.0 mmol), and potassium hydroxide (0.061 g, 1.1 mmol) in *n*-butanol (3.0 mL) were introduced, and the solution was refluxed for 4 h. The organic layer was poured into H₂O and extracted with CH₂Cl₂ (three times). The organic layer was collected and dried over anhydrous Na₂SO₄, filtered, and evaporated using a rotary evaporator under reduced pressure. The residue was subjected to column chromatography (eluent: hexane/EtOAc = 15/1), followed by recrystallization from CH₂Cl₂/MeOH (1/1), affording the title compound **2a** (0.15 g, 0.21 mmol) in 48% yield as a yellow solid.

2.5.1. 1,5-Bis[4-{2-(2,3,5,6-tetrafluoro-4-(trifluoromethyl)phenyl)ethyn-1-yl}phenoxy]pentane (**2a**)

Yield: 48% (yellow solid); M.P.: 142.8–143.3 °C; ¹H NMR (CDCl₃): δ 1.63–1.75 (m, 1H), 1.90 (quin., *J* = 6.4 Hz, 2H), 4.04 (t, *J* = 6.4 Hz, 2H), 6.91 (d, *J* = 8.8 Hz, 2H), 7.54 (d, *J* = 8.8 Hz, 2H); ¹³C NMR (CDCl₃): δ 22.7, 28.9, 67.9, 72.5, 105.5, 108.0–109.2 (m, quaternary carbon in fluorinated aromatic ring), 109.4 (t, *J* = 14.7 Hz), 112.9, 114.8, 120.8 (q, *J* = 272.8 Hz), 133.8, 144.1 (dd, *J* = 264.8, 15.4 Hz), 146.7 (dd, *J* = 257.5, 16.9 Hz), 160.6; ¹⁹F NMR (CDCl₃): δ −56.62 (t, *J* = 21.4 Hz, 3F), −135.6 to −135.8 (m, 2F), −141.5 to −141.8 (m, 2F); IR (KBr): ν 2952, 2873, 2220, 1659, 1519, 1494, 1343, 1272, 1169, 1112, 1073, 986, 837 cm^{−1}; HRMS (FAB⁺) *m/z* [M]⁺ calcd for C₃₅H₁₈F₁₄O₂: 736.1083; found: 736.1091.

2.5.2. 1,6-Bis[4-{2-(2,3,5,6-tetrafluoro-4-(trifluoromethyl)phenyl)ethyn-1-yl}phenoxy]hexane (**2b**)

Yield: 4% (white solid); M.P.: 177.0–178.0 °C; ¹H NMR (C₆D₆): δ 1.31–1.39 (m, 2H), 1.56–1.67 (m, 2H), 3.57 (t, *J* = 6.4 Hz, 2H), 6.76 (d, *J* = 8.8 Hz, 2H), 7.54 (d, *J* = 8.8 Hz, 2H); ¹³C NMR (C₆D₆): δ 26.5, 29.8, 68.5, 106.4, 113.9, 115.7, 119.7 (q, *J* = 262.6 Hz), 134.8, 143.0–146.5 (dm, *J* = 262.6 Hz), 146.0–148.8 (dm, *J* = 257.4 Hz), 161.7, three quaternary carbons were not detected due to extremely low solubility of **3b** in the deuterated solvent; ¹⁹F NMR (C₆D₆): δ −56.17 (t, *J* = 21.8 Hz, 3F), −135.9 to −136.1 (m, 2F), −141.5 to −141.9 (m, 2F); IR (KBr): ν 2947, 2222, 1604, 1520, 1495, 1396, 1344, 1172, 1073, 987, 875 cm^{−1}; HRMS (FAB⁺) *m/z* [M]⁺ calcd for C₃₆H₂₀F₁₄O₂: 750.1240; found: 750.1237.

2.5.3. 1,7-Bis[4-{2-(2,3,5,6-tetrafluoro-4-(trifluoromethyl)phenyl)ethyn-1-yl}phenoxy]heptane (**2c**)

Yield: 12% (white solid); M.P.: 133.3–134.5 °C; ¹H NMR (CDCl₃): δ 1.40–1.61 (m, 3H), 1.83 (quin., *J* = 7.2 Hz, 2H), 4.00 (t, *J* = 6.4 Hz, 2H), 6.90 (d, *J* = 8.8 Hz, 2H), 7.54 (d, *J* = 8.8 Hz, 2H); ¹³C NMR

(CDCl₃): δ 25.9, 29.0 (two signals in the heptylene spacer were overlapped), 68.1, 72.5, 105.6, 108.0–109.2 (m, quaternary carbon in a fluorinated aromatic ring), 109.5 (t, J = 18.3 Hz), 112.8, 114.8, 120.8 (q, J = 274.9 Hz), 133.8, 142.5–145.7 (dm, J = 265.5 Hz), 145.0–148.2 (dm, J = 256.7 Hz), 160.7; ¹⁹F NMR (CDCl₃): δ -56.62 (t, J = 21.8 Hz, 3F), -135.6 to -135.8 (m, 2F), -141.5 to -141.9 (m, 2F); IR (KBr): ν 2943, 2872, 2217, 1604, 1495, 1343, 1252, 1192, 1171, 1034, 988, 875 cm⁻¹; HRMS (FAB+) m/z [M]⁺ calcd for C₃₇H₂₂F₁₄O₂: 764.1396; found: 764.1397.

2.5.4. 1,8-Bis[4-{2-(2,3,5,6-tetrafluoro-4-(trifluoromethyl)phenyl)ethyn-1-yl}phenoxy]octane (**2d**)

Yield: 8% (yellow solid); M.P.: 153.1–155.0 °C; ¹H NMR (CDCl₃): δ 1.37–1.60 (m, 4H), 1.81 (quin., J = 6.8 Hz, 2H), 4.00 (t, J = 6.4 Hz, 2H), 6.91 (d, J = 8.8 Hz, 2H), 7.54 (d, J = 8.8 Hz, 2H); ¹³C NMR (CDCl₃): δ 25.9, 29.1, 29.2, 68.1, 72.5 (t, J = 3.6 Hz), 105.6, 108.0–109.2 (m, quaternary carbon in a fluorinated aromatic ring), 109.5 (t, J = 18.3 Hz), 112.8, 114.8, 120.8 (q, J = 273.6 Hz), 133.9, 142.5–145.3 (dm, J = 264.1 Hz), 145.0–148.2 (dm, J = 256.7 Hz), 160.7; ¹⁹F NMR (CDCl₃): δ -56.62 (t, J = 21.8 Hz, 3F), -135.6 to -135.8 (m, 2F), -141.5 to -141.9 (m, 2F); IR (KBr): ν 2946, 2872, 2215, 1604, 1418, 1307, 1272, 1192, 1112, 989, 873 cm⁻¹; HRMS (FAB+) m/z [M]⁺ calcd for C₃₈H₂₄F₁₄O₂: 778.1553; found: 778.1543.

2.5.5. 1,9-Bis[4-{2-(2,3,5,6-tetrafluoro-4-(trifluoromethyl)phenyl)ethyn-1-yl}phenoxy]nonane (**2e**)

Yield: 2% (white solid); M.P.: 130.0–131.2 °C; ¹H NMR (CDCl₃): δ 1.32–1.53 (m, 5H), 1.81 (quin., J = 6.4 Hz, 2H), 3.99 (t, J = 6.4 Hz, 2H), 6.90 (d, J = 8.8 Hz, 2H), 7.53 (d, J = 8.8 Hz, 2H); ¹³C NMR (CDCl₃): δ 25.9, 29.1, 29.2, 29.4, 68.2, 72.4 (t, J = 3.6 Hz), 105.6 (t, J = 3.6 Hz), 108.0–109.0 (m, quaternary carbon in a fluorinated aromatic ring), 109.5 (t, J = 15.4 Hz), 112.7, 114.8, 120.8 (q, J = 277.2 Hz), 133.8, 142.5–145.7 (dm, J = 262.6 Hz), 145.0–148.2 (dm, J = 253.8 Hz), 160.7; ¹⁹F NMR (CDCl₃): δ -56.62 (t, J = 21.8 Hz, 3F), -135.6 to -135.8 (m, 2F), -141.6 to -141.9 (m, 2F); IR (KBr): ν 2943, 2870, 2214, 1543, 1398, 1254, 1192, 1108, 1022, 986, 875 cm⁻¹; HRMS (FAB+) m/z [M]⁺ calcd for C₃₉H₂₆F₁₄O₂: 792.1709; found: 792.1719.

2.5.6. 1,10-Bis[4-{2-(2,3,5,6-tetrafluoro-4-(trifluoromethyl)phenyl)ethyn-1-yl}phenoxy]decane (**2f**)

Yield: 1% (white solid); M.P.: 146.0–147.6 °C; ¹H NMR (CDCl₃): δ 1.32–1.42 (m, 4H), 1.42–1.52 (m, 2H), 1.80 (quin., J = 6.4 Hz, 2H), 3.99 (t, J = 6.4 Hz, 2H), 6.90 (d, J = 8.8 Hz, 2H), 7.53 (d, J = 8.8 Hz, 2H); ¹³C NMR (CDCl₃): δ 26.0, 29.1, 29.3, 29.4, 68.2, 72.4 (t, J = 3.6 Hz), 105.6 (t, J = 2.9 Hz), 108.0–109.0 (m, quaternary carbon in a fluorinated aromatic ring), 109.5 (t, J = 19.8 Hz), 112.7, 114.8, 120.9 (q, J = 280.1 Hz), 133.8, 142.5–145.7 (dm, J = 264.1 Hz), 145.0–148.2 (dm, J = 255.2 Hz), 160.7; ¹⁹F NMR (CDCl₃): δ -56.63 (t, J = 21.8 Hz, 3F), -135.6 to -135.9 (m, 2F), -141.6 to -142.0 (m, 2F); IR (KBr): ν 2938, 2852, 2223, 1520, 1494, 1251, 1192, 1044, 986, 831 cm⁻¹; HRMS (FAB+) m/z [M]⁺ calcd for C₄₀H₂₈F₁₄O₂: 806.1866; found: 806.1859.

2.6. X-Ray Crystallography

A single crystal of **2a** was obtained by recrystallization from CDCl₃. The obtained single crystal was mounted on a glass fiber. X-ray diffraction patterns were recorded on a Rigaku XtaLabMini diffractometer equipped with a VariMax Mo optic system (λ = 1.54187 Å) and a Pilatus P200 detector. The reflection data were processed with *CrysAlisPro* (ver. 1.171.38.46, Rigaku Oxford Diffraction, 2015). The structures were solved by a directed method (*SHELXT-2014/5*) and *SHELXL-2014/7* programs [36]. The crystallographic data were deposited into the Cambridge Crystallographic Data Centre (CCDC) database (CCDC 2011588 for **2a**). These data can be obtained free of charge from the CCDC via www.ccdc.cam.ac.uk/data_request/cif.

2.7. Computations

Density functional theory (DFT) calculations were carried out using the Gaussian 16 (Rev. B.01) suite of programs [37]. Geometry optimizations were performed at the CAM-B3LYP/6-31+G(d)

level of theory [38,39] with an implicit solvation model, namely, the conductor-like polarizable continuum model (CPCM) for CH_2Cl_2 [40–42]. The vertical electronic transitions were calculated using a time-dependent (TD)-DFT method at the same level of theory.

2.8. Photophysical Measurements

Ultraviolet–visible (UV–vis) absorption spectra were recorded on a V-500 absorption spectrometer (JASCO, Tokyo). Samples for UV–vis measurements were prepared by dissolving dyads **2** in CH_2Cl_2 ($1.0 \times 10^{-5} \text{ mol L}^{-1}$), and the CH_2Cl_2 solution was transferred into quartz cuvettes (optical path length: 1 cm). Steady-state PL spectra in solution and crystalline powder states as well as quantum yields were acquired using an absolute PL quantum yield measurement system (Hamamatsu Photonics, C11347-01). A solution-phase sample ($1.0 \times 10^{-6} \text{ mol L}^{-1}$) was used for PL measurements using quartz cuvettes (optical path length: 1 cm). The excitation wavelength (λ_{ex}) corresponded to the maximum absorption wavelength. Crystalline powder or ground samples for PL measurements were placed above a quartz Petri dish and characterized using a calibrated integrating sphere.

3. Results and Discussion

3.1. Theoretical Molecular Assessment

In order to assess the validity of our molecular design of fluorinated tolane dyads **2**, we initially carried out theoretical quantum chemical calculations for the **2** substrates with pentylene and hexylene linkages, viz., **2a** and **2b**, respectively, as well as for the parent analog **1b** by employing a DFT method using the Gaussian 16 (Rev. B.01) software. The optimized molecular geometry was elucidated by theoretical calculations at the CAM-B3LYP/6-31+G(d) level of theory with a CPCM for CH_2Cl_2 and had no imaginary frequency. Theoretical vertical transitions were also calculated using the time-dependent (TD)-DFT method at the same level of theory. The optimized geometries, highest occupied molecular orbital (HOMO), and lowest unoccupied molecular orbital (LUMO) for the fluorinated tolane **1b** and the tolane dyads **2a** and **2b** are shown in Figure 2. The calculated theoretical parameters are summarized in Table 1.

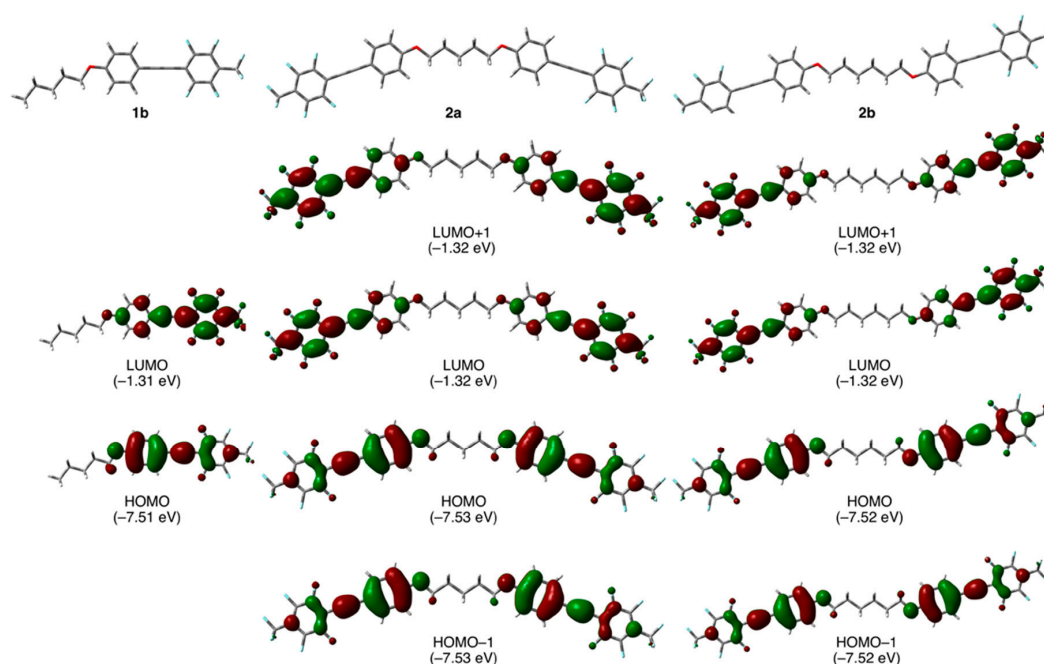


Figure 2. Optimized geometries of **1b**, **2a**, and **2b** and their molecular orbital distributions (orbital energy) involving vertical electronic transitions obtained by theoretical chemical calculations at the CAM-B3LYP/6-31+G(d) level of theory.

Table 1. Theoretical parameters of **1b**, **2a**, and **2b** obtained by DFT calculations. ¹.

Molecule	Dipole Moment (D)	HOMO (eV)	LUMO (eV)	Theoretical Transition ²	Transition Energy (nm) ²	$f^{2,3}$
1b	7.12	−7.51	−1.31	HOMO → LUMO (91%)	315	1.368
2a	1.60	−7.53	−1.32	HOMO−1 → LUMO (45%) HOMO → LUMO + 1 (45%)	316	2.581
2b	0	−7.52	−1.32	HOMO−1 → LUMO (45%) HOMO → LUMO + 1 (45%)	315	2.795

¹ Calculated using Gaussian 16 (rev. B.01) with DFT method (CAM-B3LYP/6-31+G(d) level of theory). ² Obtained from time-dependent (TD)-DFT calculations at the same level of theory. ³ Calculated oscillator strength.

As can be seen in Figure 2, parent fluorinated tolane **1b** had a linear geometry for the most stable conformation. In contrast to **1b**, dyad **2a** connected with an odd-numbered alkylene linkage, viz., $-(CH_2)_5-$ and had a bent geometry in which the two tolane scaffolds occupied a syn-periplanar arrangement, whereas dyad **2b** with an even-numbered alkylene linkage, viz., $-(CH_2)_6-$, was found to form a zig-zag geometry with an antiperiplanar relationship between the two tolane moieties. Accordingly, it was expected that switching the molecular structure from the parent tolane moiety to the dyads connected with an alkylene linkage would provide a dynamic effect on the molecular aggregated structures.

Focusing on the electronic structures, subsequently, in the case of **1b**, the orbital lobe of the HOMO was relatively localized over the electron-rich aromatic ring attached to an alkoxy substituent, whereas the LUMO lobe existed over the electron-deficient fluorinated aromatic ring. The relative localization of the HOMO and LUMO lobes in **1b** caused a larger electron-density distribution, resulting in a large molecular dipole moment (7.12 D). Dyads **2a** and **2b** with two fluorinated tolane scaffolds also possessed molecular orbitals with relatively localized electron-density at the electron-rich aromatic ring for the HOMO or electron-deficient counterpart of the LUMO. Interestingly, however, the molecular dipole moment of **2a** and **2b** was found to be relatively or completely cancelled by the two oppositely directed fluorinated tolane moieties substituted in both molecular terminals, resulting in only 1.60 D for **2a** with a bent geometry and 0 D for **2b** with a zig-zag geometry. The large difference between the molecular dipole moments of the parent **1b** and dyads **2a** and **2b** is also possibly attributable to the distinct photophysical behavior. Both the orbital energies for HOMO and HOMO−1 were calculated to be almost identical: −7.53 eV for **2a** and −7.52 eV for **2b**. The LUMO and LUMO + 1 orbital energies were also the same: −1.32 eV for **2a** and **2b**. These results indicate that HOMO/HOMO−1 and LUMO/LUMO + 1 for dyads **2a** and **2b** are degenerate orbitals, respectively.

As a consequence, the present molecular design for the fluorinated tolane dyads **2** connected with an alkylene linkage would provide a large difference in not only the molecular aggregated structures but also the molecular orbitals of the parent fluorinated tolane monad **1**, which would result in a unique photophysical behavior.

3.2. Synthesis and Crystal Structure

On the basis of the theoretical assessments, we started with the synthesis of the fluorinated tolane dyads **2a** and **2b** connected with a pentylene or a hexylene linkage according to the synthetic route shown in Scheme 1. Thus, the reaction of 4-(methoxymethoxy)phenylacetylene (**3**), prepared from 4-bromophenol according to a reported procedure [33–35], with *n*-butyllithium in THF at 0 °C for 1 h, followed by the addition of octafluorotoluene (1.5 equiv.) proceeded well to afford the corresponding methoxymethoxy-substituted fluorinated tolane **4** in 82% yield through an addition–elimination process [27]. On treating **4** with concentrated hydrochloric acid in a mixed solvent (THF/MeOH *v/v* = 1/1) at 25 °C for 22 h, the methoxymethyl fragment was successfully removed to provide the corresponding hydroxy-substituted fluorinated tolane **5** in 86% yield. Subsequent Williamson etherification of **5** with 1,5-dibromopentane (**a**, 0.5 equiv.) in the presence of 1.0 equiv. of potassium hydroxide in *n*-butanol at 130 °C for 4 h [43] was used to provide the corresponding fluorinated tolane

dyad **2a** with a pentylene linkage in 48% yield after subjecting the sample to column chromatography (hexane/EtOAc = 15/1) and recrystallization from CH₂Cl₂/MeOH (*v/v* = 1/1). Using a similar protocol using the corresponding 1,*n*-dibromoalkane (*n* = 6–10), desired fluorinated tolane dyads **2b–f** with an alkylene linkage were successfully obtained in low yield due to the difficulty of separation from a mixture of various side products, for example, mono-etherification products. After purification, the fluorinated tolane dyads **2a–f** were proven to be pure enough to evaluate their photophysical behavior in their spectroscopic assessments, that is, NMR for ¹H, ¹³C, and ¹⁹F, IR, and HRMS.

Among **2a–f** in hand, **2a** with a pentylene linkage successfully formed single crystals appropriate for X-ray crystallographic analysis via recrystallization from CDCl₃. Although the preparation of single crystals for other analogs **2b–f** was repeatedly attempted, it remained unsuccessful. Figure 3 shows the crystal and packing structures of **2a**.

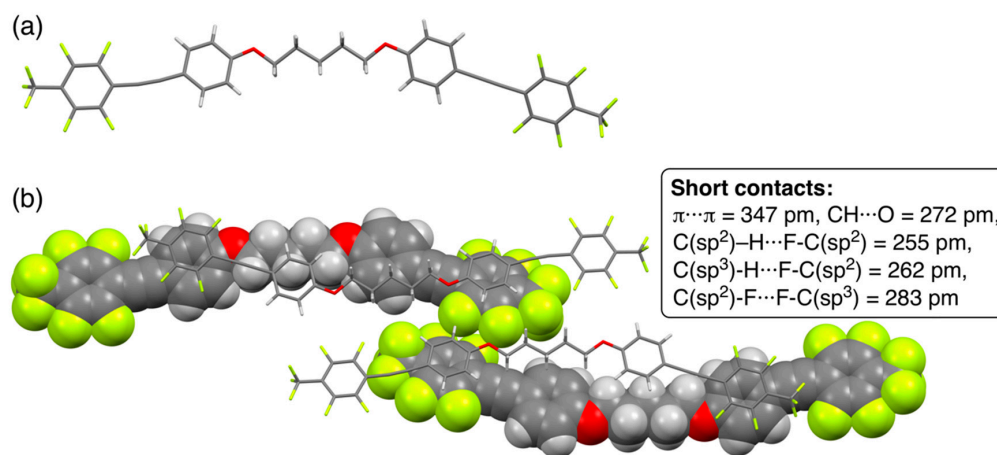


Figure 3. (a) Crystal structure of **2a** and (b) packing structures in a unit cell. Short contacts, which indicate interatomic distances below the sum of van der Waals radii, are also shown. van der Waals radius for carbon (C): 170 pm, hydrogen (H): 120 pm, oxygen (O): 152 pm, and fluorine (F): 147 pm [44].

Dyad **2a** connected with a pentylene linkage formed single crystals in the monoclinic *P* 2₁/*n* space group and had eight formula units in a unit cell. Similar to theoretical results, the structure of **2a** in the crystal was found to have a bent geometry in which the pentylene linkage formed an all-trans conformation (Figure 3a). On carefully observing the packing structures for **2a** shown in Figure 3b, the bent molecules were noted to alternately pile on one another in an anti-parallel direction. The piled structures were constructed through intermolecular π/π interactions with a short contact of the interfacial $\pi \cdots \pi$ distance (347 pm) between electron-deficient fluorinated aromatic rings and electron-rich alkoxy-substituted aromatic rings, according to the van der Waals radius of the carbon atom (170 pm) reported by Bondi [44]. In the packing structures, additionally, plural intermolecular interactions with short contacts between CH \cdots O (272 pm), CH \cdots F (255–262 pm), and F \cdots F (283 pm) were observed, which could be recognized as hydrogen bonding as well as F/F interactions [45].

Considering the crystal structures of dyad **2a**, it was anticipated that dyads **2a**, **2c**, and **2e**, with an odd number of alkylene linkages, could constitute a bent structure in the aggregated states, and dyads **2b**, **2d**, and **2f**, with an even number of alkylene linkages, could form a zig-zag structure.

3.3. Photophysical Behavior in a Solution State

For freshly prepared dyads **2a–f** connected with various alkylene linkages, we initially investigated the photophysical behavior in a dichloromethane (CH₂Cl₂) solution. The measurement sample was prepared by dissolving crystalline powder **2a–f** in CH₂Cl₂ to a concentration of 1.0×10^{-5} mol L⁻¹ for UV–vis absorption and a concentration of 1.0×10^{-6} mol L⁻¹ for PL measurements. The acquired

UV-vis and PL spectra are illustrated in Figure 4a. Their photophysical parameters are also summarized in Table 2.

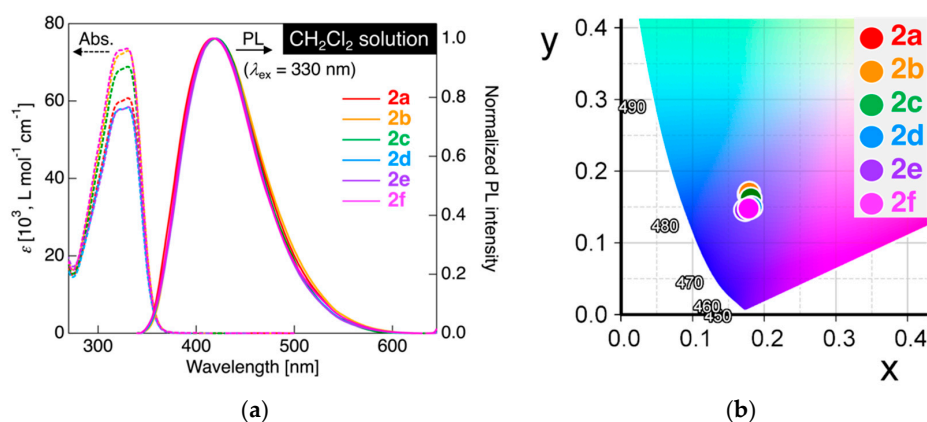


Figure 4. (a) UV-vis absorption (dashed line) and PL spectra (solid line) for **2a–f** in CH₂Cl₂. Concentration: 1.0×10^{-5} mol L⁻¹ for UV-vis and 1.0×10^{-6} mol L⁻¹ for PL measurements. Excited at 330 nm light. (b) Commission Internationale de l’Eclairage (CIE) color diagram for PL of **2a–f** in CH₂Cl₂.

Table 2. Photophysical parameters of **2a–f** in CH₂Cl₂ solution.

Dyad	λ_{abs} [nm] ($\epsilon \times 10^{-3}$ [L mol ⁻¹ cm ⁻¹]) ¹	λ_{PL} [nm] ² (Φ_{PL}) ³
2a	321sh (59.7), 331 (60.7)	417 (0.10)
2b	321sh (71.8), 330 (73.0)	420 (0.10)
2c	321sh (67.9), 330 (68.9)	420 (0.10)
2d	321sh (57.8), 330 (58.3)	419 (0.09)
2e	321sh (57.7), 331 (58.5)	419 (0.09)
2f	321sh (73.0), 329 (73.6)	417 (0.09)

¹ Concentration of solution: 1.0×10^{-5} mol L⁻¹. ² Concentration of solution: 1.0×10^{-6} mol L⁻¹. Excited at 330 nm light. ³ Measured using a calibrated integrating sphere sh: shoulder.

In the UV-vis absorption experiments, **2a** connected with a pentylene linkage showed a single absorption band with absorption maximum wavelength (λ_{abs}) at 331 nm, along with a shoulder peak at 321 nm. Similar to the UV-vis absorption behavior of **2a**, other dyads **2b–f** also displayed absorption spectra with λ_{abs} at 321 and 329–331 nm. This analogy of the UV-vis absorption spectra for **2a–f** with a parent monad **1a** (λ_{abs} = 329 nm) [27] clearly indicated that the length of the alkylene linkage did not cause a significant change in the electronic structures in the solution state. To gain more information on the electronic transition in the absorption behavior, we also performed TD-DFT calculations at the same level of theory (CAM-B3LYP/6-31+G(d) with a CPCM for CH₂Cl₂) for dyads **2a** and **2b** as a representative example. Both **2a** and **2b** showed an allowed electronic transition involving HOMO → LUMO+1 (45%) and HOMO–1 → LUMO (45%) with a large oscillator strength (f). In the case of the parent monad **1b**, however, it was calculated that the allowed electronic transition involving HOMO → LUMO had a smaller value of f . The large f values in **2a** and **2b** stem from the two possible transitions from degenerate HOMO/HOMO–1 → LUMO/LUMO+1. Comparing the UV-vis absorption spectrum of **1a** [27], it was proven that approximately two-fold larger molar extinction coefficient (ϵ) for dyads **2a–f**, rather than that for **1a**. As mentioned before, the molecular orbital distributions among **1b**, **2a**, and **2b** were quite similar in which the orbital lobe covered the electron-rich aromatic ring in the HOMO and the electron-deficient fluorinated aromatic ring in the LUMO (Figure 2); the electronic transition in the absorption process could be assigned to the intramolecular charge transfer (ICT) transition [27].

Upon irradiating the CH_2Cl_2 solution of **2a** with excitation light at 330 nm, which is close to the λ_{abs} , **2a** showed PL with a single PL band at the maximum PL wavelength (λ_{PL}) of approximately 417 nm. On measuring the absolute PL efficiency (Φ_{PL}) using an integrating sphere, the Φ_{PL} of **2a** in CH_2Cl_2 was found to be as low as 0.10. When PL measurements were performed for other dyads **2b–f** in CH_2Cl_2 solution, all analogs also exhibited a weak PL (Φ_{PL} = up to 0.10) with a single PL band at λ_{PL} in the range of 417–420 nm. The PL color was quantitatively shown using the Commission Internationale de l’Eclairage (CIE) definition calculated from the observed PL spectra, although the PL in CH_2Cl_2 under UV irradiation (λ_{ex} = 365 nm) was not clearly visible due to low Φ_{PL} . As shown in Figure 4b, the CIE color coordinates (x , y) of the PL color were (0.178, 0.168) for **2a**, (0.179, 0.170) for **2b**, (0.181, 0.162) for **2c**, (0.182, 0.150) for **2d**, (0.173, 0.146) for **2e**, and (0.178, 0.148) for **2f**, which clearly indicates that the PL color of **2a–f** in CH_2Cl_2 solution was almost consistently deep blue. Additionally, it was proven that the PL behavior of dyads **2a–f** was quite similar to that of the parent tolane **1a** reported previously [27], namely, it could be rationally explained that the PL of dyads **2a–f** was attributable to radiative deactivation through ICT transition.

3.4. Photophysical Behavior in Crystalline Powder State

In our previous study [27], the parent tolane derivative **1a** was found to exhibit aggregation-induced emission enhancement; **1a** weakly emitted PL in a dilute solution state but showed significantly enhanced PL intensity with the formation of molecular aggregates. Based on the preliminary result of **1a**, our attention was then directed toward the PL behavior of dyads **2a–f** in the crystalline powder states. Figure 5 shows the PL spectra, photographs showing PL under UV irradiation, and the CIE color diagram for their PL colors. The photophysical data obtained are summarized in Table 3.

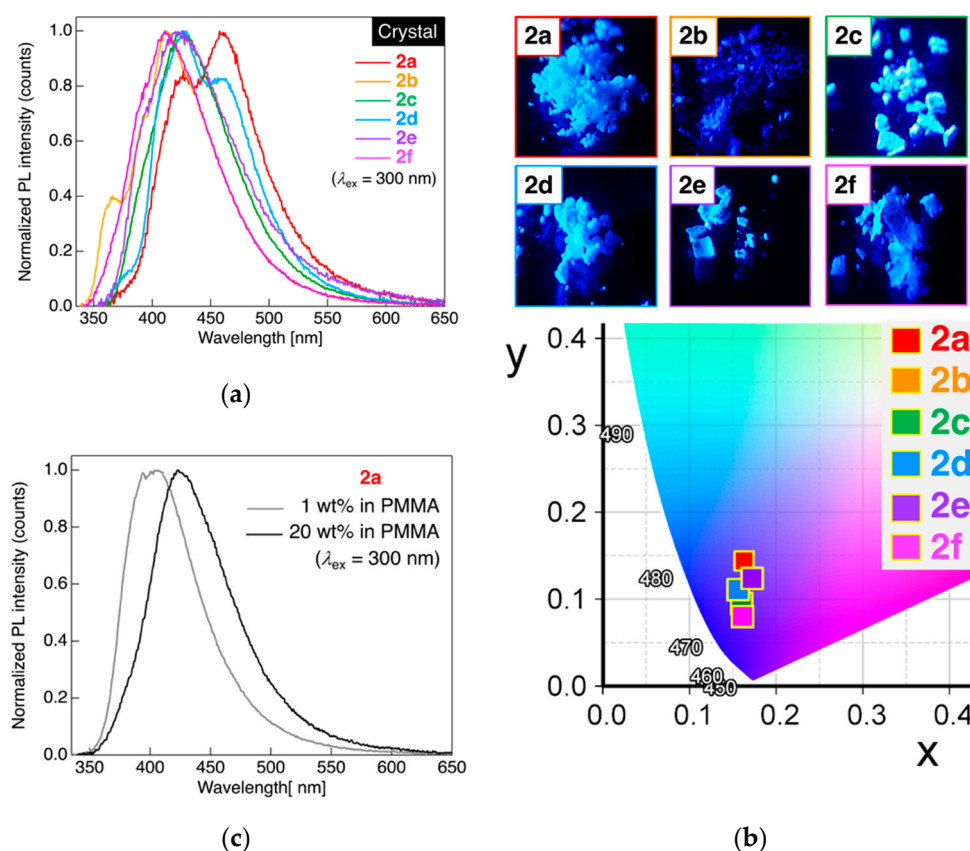


Figure 5. (a) PL spectra of dyads **2a–f** in crystalline powder states. Excited at 300 nm light. (b) Photographs of the PL behavior of **2a–f** in crystalline powder states and the CIE color diagram. (c) PL spectra of **2a** blended in poly(methyl methacrylate). Excited at 300 nm light.

Table 3. Photophysical parameters of **2a–f** in the molecular aggregated states.

Dyad	States	λ_{PL} [nm] ¹ (Φ_{PL}) ²
2a	Crystalline	427, 458 (0.17)
	PMMA (1 wt % of 2a)	406 (0.39)
	PMMA (20 wt % of 2a)	423 (0.23)
	Ground	432 (0.25)
2b	Crystalline	366, 412 (0.41)
	Ground	418 (0.56)
2c	Crystalline	427 (0.45)
2d	Crystalline	428, 460 (0.30)
	Ground	433, 458 (0.48)
2e	Crystalline	420 (0.22)
2f	Crystalline	411 (0.42)

¹ Excited at 300 nm light. ² Measured using a calibrated integrating sphere PMMA: poly(methyl methacrylate).

When determining the PL behavior of dyad **2a** connected to a pentylene linkage in crystalline powder states at 25 °C, two PL bands with λ_{PL} at approximately 427 and 458 nm were observed, which were quite different from the results noted in a dilute solution state, as shown in Figure 4a. The PL color of **2a** in the crystalline powder state was blue to the naked eye under UV irradiation (λ_{ex} = 365 nm) with a CIE coordinate, $(x, y) = (0.163, 0.144)$. Considering the λ_{PL} and PL band shape for monad **1a** in crystalline state [27], the present dyad **2a** showed a distinct PL band shape with a slight long-wavelength shift of λ_{PL} ; it was strongly anticipated that the dyad with an alkylene linkage formed significantly different molecular aggregates in the crystalline powder states. Dyad **2b** with a hexylene linkage also showed deep blue PL ($(x, y) = (0.161, 0.08)$) with a major PL band at approximately 412 nm of λ_{PL} , along with a minor PL band at approximately 366 nm of λ_{PL} . Dyad **2d** with an octylene linkage was observed to emit blue PL with two PL bands at approximately 428 nm and 460 nm of λ_{PL} , whereas other analogs, viz., dyads **2c** with a heptylene linkage, **2e** with a nonylene linkage, and **2f** with a decylene linkage, exhibited blue to deep blue PL only with a single band at approximately 411–427 nm of λ_{PL} . In contrast to the PL behavior of **2a–f** in CH_2Cl_2 solution as mentioned above, the PL spectral shape as well as λ_{PL} were found to significantly change with the alkylene linkage length. Based on our prior knowledge on PL behavior in crystalline states [22–28], the large differences among PL behavior of **2a–f** in the crystalline powder state was likely attributable to the distinct intermolecular interactions between neighboring molecules, although no odd–even effect was noted in the PL behavior of the crystalline powder state samples of dyads **2a–f**. In sharp contrast to the Φ_{PL} of **2a–f** in the solution state, the Φ_{PL} of **2a–f** in the crystalline powder state was found to increase up to 0.56, which was possibly due to the significant suppression of non-radiative deactivation induced by molecular motions by the formation of molecular aggregates via intermolecular interactions.

To confirm the origin of the two PL bands in the crystalline powdered **2a**, we investigated the PL behavior of **2a** dispersed in poly(methyl methacrylate) (PMMA)-film in which the concentration of **2a** was either 1 wt% or 20 wt%. As shown in Figure 5c, the PL spectrum of 1 wt% of **2a** in the PMMA film was found to show a single PL band at 406 nm of λ_{PL} , which significantly shifted to the short-wavelength region by approximately 20 nm in comparison with the PL band in the crystalline powder state. Increasing the mass concentration of **2a** in the PMMA film from 1 wt% to 20 wt% caused a long-wavelength shift of the PL band, resulting in a single PL band at 423 nm of λ_{PL} . Comparing Φ_{PL} in both 1 wt% and 20 wt% of **2a** in PMMA film, Φ_{PL} in 1 wt% of **2a** in PMMA (0.39) was found to be higher than that in 20 wt% of **2a** in PMMA (0.23), which reasonably decreased the Φ_{PL} at higher concentrations due to the concentration quenching effect. In order to clarify the PL behavior, we demonstrated an experiment in mixed solvent solutions of THF and H_2O . As shown in Figure S33 (Supporting Information), the PL intensity approximately increased five-fold on adding 10% H_2O respect to 90% THF, together with a slight red-shift of λ_{PL} by 45 nm, although the formation of precipitate was not observed at all. The results likely indicate that the PL may stem from the rigidification of dyads **2a**

in THF/H₂O mixed solvents. Interestingly, the PL changed in color from greenish blue to light blue when the precipitate of molecular aggregates formed in a 50/50 composition of THF/H₂O. When the H₂O fraction reached 70%, the highest Φ_{PL} of 0.50 was observed, which may be attributable to an aggregation-induced emission enhancement. Judging from the tendency of both λ_{PL} and Φ_{PL} , it can be assumed that the PL band of crystalline powdered **2a** in the long-wavelength region stemmed from an emission from small-sized molecular aggregates or crystal surface defects [46,47].

3.5. Mechanochromic PL Behavior of **2a**, **2b**, and **2d** after Mechanical Stimulus

For dyads **2a**, **2b**, and **2d**, which possessed two distinct PL bands, we chose to investigate the behavior noted upon providing a mechanical stimulus, which is used to assess the mechanochromic PL behavior of PL materials. Thus, we measured the PL behavior of dyads **2a**, **2b**, and **2d** after applying mechanical grinding in a mortar. Figure 6 shows the PL spectra obtained from the as-prepared PL spectra of the crystalline powder sample and the associated photophysical parameters are provided in Table 3.

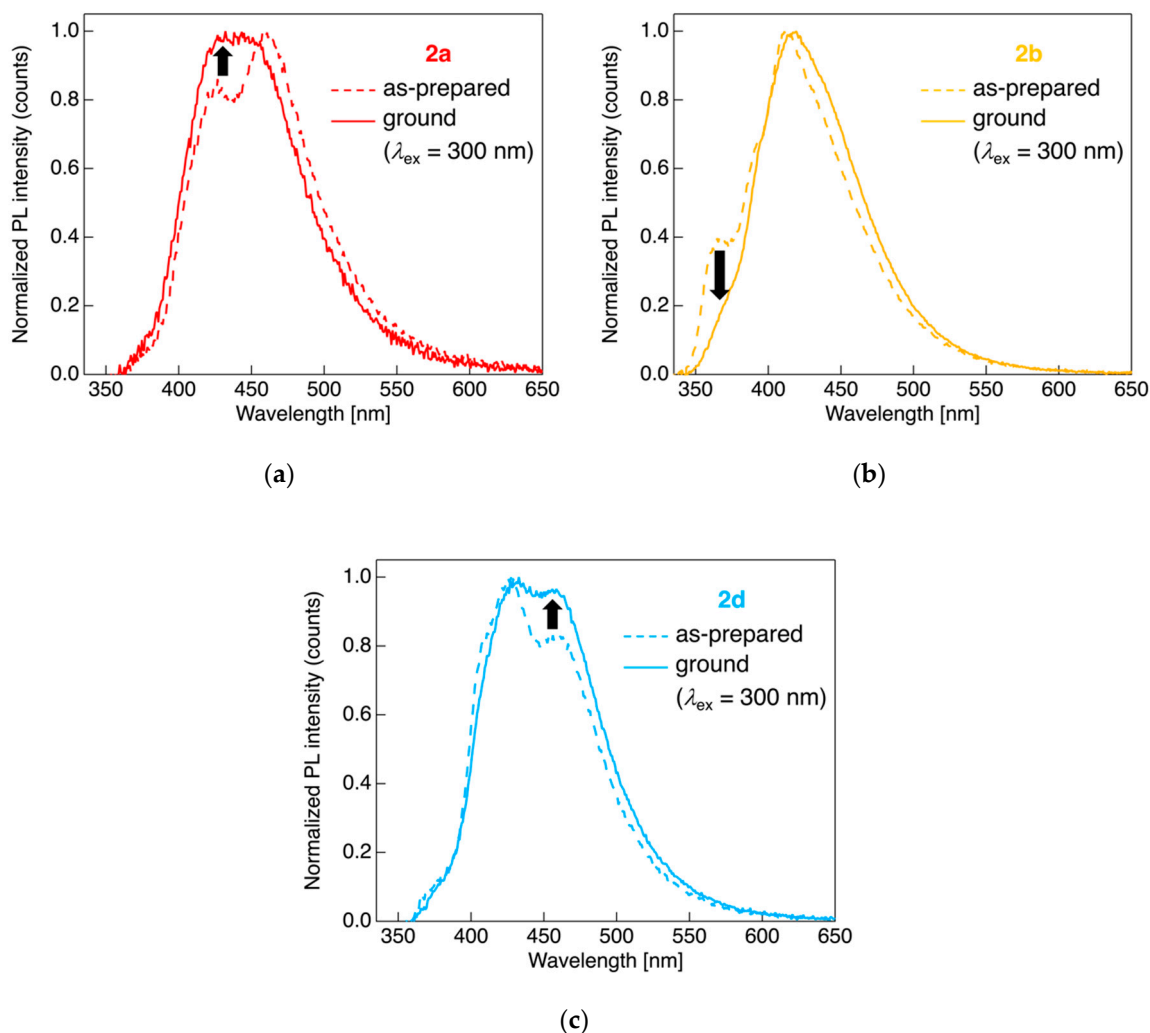


Figure 6. PL spectra of dyads (a) **2a**, (b) **2b**, and (c) **2d** for the as-prepared crystalline powder sample (dashed line) and for the ground sample after applying a mechanical stimulus (solid line). Excited at 300 nm light.

When the crystalline powdered **2a** was ground in a mortar, spectral change occurred for the PL; the intensity of the PL band in the short-wavelength region increased and finally a broad single PL

band was observed after applying a mechanical stimulus; the dyad **2a** likely deconstructed molecular aggregates owing to mechanical stress, leading to an increase in the PL intensity originating from monomer emission. Although the PL behavior of dyads **2b** and **2d** also changed on the application of a mechanical stimulus in the mortar, in contrast to the aforementioned dyad **2a**, decreased PL band intensity in the short-wavelength region in case of **2b** or increased PL intensity in the long-wavelength region in the case of **2d** was observed; application of the mechanical stimulus to the as-prepared **2b** and **2d** samples contributed to amorphization of the powders through grinding, resulting in an increase in the PL band intensity and broadening of the PL band stemming from the aggregate emission. When **2a** was recrystallized after thermal heating-cooling processes, a slight long-wavelength shift (Figure S35D) was observed for the PL. Overall, it can be concluded that the studied fluorinated tolane dyads connected to an alkylene linkage can serve as stimulus-responsive light-emitting molecules, although the alteration of PL parameters, such as the color and the λ_{PL} , is quite limited.

4. Conclusions

In conclusion, we designed and synthesized novel fluorinated tolane dyads, which consist of fluorinated π -conjugated scaffolds with an intense crystalline state light-emitting property and flexible alkylene linkage that can dynamically change molecular geometries as well as aggregated structures in the crystalline powder state. A series of fluorinated tolane dyads with various lengths of linkages, which were prepared using a facile three-step protocol from readily available 4-(2-methoxymethoxy)phenylacetylene, showed absorption and blue photoluminescence (PL) in dilute CH_2Cl_2 solution, but the PL efficiency was found to be low (Φ_{PL} = up to 0.1). The absorption and PL spectra of the dyads connected with linkages of various lengths were found to be almost identical. These results indicate that, in the dispersed system, the electronic transition between the ground and excited states is strongly attributable to the electron-density distribution of the fluorinated π -conjugated scaffold. In contrast to the PL behavior in dilute solutions, irradiation of UV light into the fluorinated tolane dyads in the crystalline powder states brought about significant change in the PL spectral shape for a variety of alkylene linkages, resulting in blue to deep blue PL emissions with a significant enhancement of Φ_{PL} (up to 0.56). Owing to the PL behavior of the dyad dispersed in poly(methyl methacrylate) film, the fluorinated tolane dyads were concluded to exhibit dual monomer and aggregate emissions. On applying a mechanical stimulus to the crystalline powder tolane dyads with dual emissions, an increase in the intensity of the PL band at the short-wavelength region occurred, owing to monomer emission for the dyads with an odd number of alkylene linkages, whereas the dyads with an even number of alkylene linkages showed an increase in the PL band intensity at the other long-wavelength region, owing to aggregate emission. Thus, the fluorinated tolane dyads with an alkylene linkage that were studied in this work were demonstrated to show dual emission character that can change the PL behavior with a mechanical stimulus, which would be promising for an application in PL sensing materials triggered by an external stimulus.

Supplementary Materials: The following are available online at <http://www.mdpi.com/2073-4352/10/8/711/s1>, Figure S1–S24: NMR spectra of **2a–f**, Table S1: Theoretical photophysical data obtained by TD-DFT calculations, Figure S25–S30: Optimized structures for **1**, **2a**, and **2b**, Table S2–S7: Cartesian coordinates of **1**, **2a**, and **2b**, Figure S31: crystal and packing structures of **2a**, Table S8: crystallographic data of **2a**, Figure S32–S35: Absorption (excitation) and PL spectra of **2a–f**.

Author Contributions: Conceptualization, S.Y.; Methodology, S.Y.; Validation, S.Y., E.U. and T.K. (Tsutomu Konno); Investigation, S.Y., E.U., T.A., T.K. (Toshio Kubota) and T.K. (Tsutomu Konno); Writing—Original Draft Preparation, S.Y. and E.U.; Writing—Review and Editing, S.Y., E.U., T.A., T.K. (Toshio Kubota) and T.K. (Tsutomu Konno); Visualization, S.Y. and E.U.; Supervision, S.Y.; Project administration, S.Y.; Funding acquisition, S.Y. All authors have read and agreed to the published version of the manuscript.

Funding: This research was funded by JSPS KAKENHI through a Grant-in-Aid for Scientific Research (C), grant number JP18K05262.

Conflicts of Interest: The authors declare no conflict of interest.

References

- Kundu, S.; Sk, B.; Pallavi, P.; Giri, A.; Patra, A. Molecular engineering approaches toward all-organic white light emitting materials. *Chem. Eur. J.* **2020**, *26*, 5557–5582. [[CrossRef](#)] [[PubMed](#)]
- Chen, Z.; Ho, C.-L.; Wang, L.; Wong, W.-Y. Single-molecular white-light emitters and their potential WOLED applications. *Adv. Matter.* **2020**, *32*, 1903269. [[CrossRef](#)] [[PubMed](#)]
- Singh, D.; Bhagwan, S.; Saini, R.K.; Nishal, V.; Singh, I. Development in organic light-emitting materials and their potential applications. In *Advanced Magnetic and Optical Materials*; Tiwari, A., Iyer, P.K., Kumar, V., Swart, H., Eds.; Scrivener Publishing: Beverly, MA, USA, 2017; pp. 473–520.
- Shen, Q.; Wang, S.; Yang, N.-D.; Zhang, C.; Wu, Q.; Yu, C. Recent development of small-molecule organic fluorophores for multifunctional bioimaging in the second near-infrared window. *J. Lumines.* **2020**, *225*, 11738. [[CrossRef](#)]
- Shaikh, S.; Wang, Y.; ur Rehman, F.; Jiang, H.; Wang, X. Phosphorescent Ir(III) complexes as cellular staining agents for biomedical molecular imaging. *Coord. Chem. Rev.* **2020**, *416*, 213344. [[CrossRef](#)]
- Wang, Y.; Nie, J.; Fang, W.; Yang, L.; Hu, Q.; Wang, Z.; Sun, J.Z.; Tang, B.Z. Sugar-based aggregation-induced emission luminogens: Design, structures, and applications. *Chem. Rev.* **2020**, *120*, 4534–4577. [[CrossRef](#)]
- Yersin, H. (Ed.) *Highly Efficient OLEDs: Materials Based on Thermally Activated Delayed Fluorescence*; Wiley-VCH: Weinheim, Germany, 2018.
- Bui, T.-T.; Goubard, F.; Ibrahim-Ouali, M.; Gigmes, D.; Dumur, F. Recent advances on organic blue thermally activated delayed fluorescence (TADF) emitters for organic light-emitting diodes (OLEDs). *Beilstein J. Org. Chem.* **2018**, *14*, 282–308. [[CrossRef](#)]
- Ostroverkhova, O. Organic optoelectronic materials: Mechanisms and applications. *Chem. Rev.* **2016**, *116*, 13279–13412. [[CrossRef](#)]
- Gaspar, D.J.; Polikarpov, E. *OLED Fundamentals: Materials, Devices, and Processing of Organic Light-Emitting Diodes*; CRC Press: Boca Raton, FL, USA, 2015.
- Thomas, S.W.; Joly, G.D.; Swager, T.M. Chemical sensors based on amplifying fluorescent conjugated polymers. *Chem. Rev.* **2007**, *107*, 1339–1386. [[CrossRef](#)]
- Li, H.; Li, B.S.; Tang, B.Z. Molecular design, circularly polarized luminescence, and helical self-assembly of chiral aggregation-induced emission molecules. *Chem. Asian J.* **2019**, *14*, 674–688. [[CrossRef](#)]
- He, Z.; Ke, C.; Tang, B.Z. Journey of aggregation-induced emission research. *ACS Omega* **2018**, *3*, 3267–3277. [[CrossRef](#)]
- Mei, J.; Leung, N.L.C.; Kwok, R.T.K.; Lam, J.W.Y.; Tang, B.Z. Aggregation-induced emission: Together we shine, united we soar! *Chem. Rev.* **2015**, *21*, 11718–11940. [[CrossRef](#)] [[PubMed](#)]
- Zhao, Z.; He, B.; Tang, B.Z. Aggregation-induces emission of siloles. *Chem. Sci.* **2015**, *6*, 5347–5365. [[CrossRef](#)] [[PubMed](#)]
- Chen, J.; Peng, Q.; Peng, X.; Han, L.; Wang, X.; Wang, J.; Zeng, H. Recent advances in mechano-responsive hydrogels for biomedical applications. *ACS Appl. Polym. Mater.* **2020**, *2*, 1092–1107. [[CrossRef](#)]
- Praveen, V.K.; Vedhanarayanan, B.; Mal, A.; Mishra, R.K.; Ajayaghosh, A. Self-Assembled Extended π -Systems for Sensing and Security Applications. *Acc. Chem. Res.* **2020**, *53*, 496–507. [[CrossRef](#)]
- Sagara, Y.; Takahashi, K.; Nakamura, T.; Tamaoki, N. Mechanochromic Luminescence from crystals consisting of intermolecular hydrogen-bonded sheets. *Chem. Asian J.* **2020**, *15*, 478–482. [[CrossRef](#)]
- Isoda, K.; Matsubara, M.; Ikenaga, A.; Akiyama, Y.; Mutoh, Y. Reversibly/irreversibly stimuli-responsive inks based on N-heteroacene liquids. *J. Mater. Chem. C* **2019**, *7*, 14075–14079. [[CrossRef](#)]
- Seki, T.; Ida, K.; Ito, H. A meta-diisocyanide benzene-based aryl gold isocyanide complex exhibiting multiple solid-state molecular arrangements and luminescent mechanochromism. *Mater. Chem. Front.* **2018**, *2*, 1195–1200. [[CrossRef](#)]
- Kobayashi, A.; Kato, M. Stimuli-responsive luminescent copper(I) complexes for intelligent emissive devices. *Chem. Lett.* **2017**, *46*, 154–162. [[CrossRef](#)]
- Yamada, S.; Mitsuda, A.; Adachi, K.; Hara, M.; Konno, T. Development of light-emitting liquid-crystalline polymers with a pentafluorinated bistolane-based luminophore. *New J. Chem.* **2020**, *44*, 5684–5691. [[CrossRef](#)]

23. Morita, M.; Yamada, S.; Agou, T.; Kubota, T.; Konno, T. Luminescence tuning of fluorinated bistolanes via electronic or aggregated-structure control. *Appl. Sci.* **2019**, *9*, 1905. [\[CrossRef\]](#)
24. Yamada, S.; Miyano, K.; Agou, T.; Kubota, T.; Konno, T. 2-Chloroalkoxy-substituted pentafluorinated bistolanes as novel light-emitting liquid crystals. *Crystals* **2019**, *9*, 195. [\[CrossRef\]](#)
25. Yamada, S.; Morita, M.; Konno, T. Multi-color photoluminescence induced by electron-density distribution of fluorinated bistolane derivatives. *J. Fluor. Chem.* **2017**, *202*, 54–64. [\[CrossRef\]](#)
26. Yamada, S.; Miyano, K.; Konno, T.; Agou, T.; Kubota, T.; Hosokai, T. Fluorine-containing bistolanes as light-emitting liquid crystalline molecules. *Org. Biomol. Chem.* **2017**, *15*, 5949–5958. [\[CrossRef\]](#) [\[PubMed\]](#)
27. Morita, M.; Yamada, S.; Konno, T. Fluorine-induced emission enhancement of tolans via formation of tight molecular aggregates. *New J. Chem.* **2020**, *44*, 6704–6708. [\[CrossRef\]](#)
28. Yamada, S.; Nishizawa, A.; Morita, M.; Hosokai, T.; Okabayashi, Y.; Agou, T.; Hosoya, T.; Kubota, T.; Konno, T. Synthesis and characterization of bent fluorine-containing donor- π -acceptor molecules as intense luminophores with large Stokes shifts. *Org. Biomol. Chem.* **2019**, *17*, 6911–6919. [\[CrossRef\]](#)
29. Grunwald, M.A.; Haenle, J.C.; Kreß, K.C.; Forschner, R.; Wöhrle, T.; Frey, W.; Giesselmann, F.; Laschat, S. Mesomorphic properties of cyanobiphenyl dimers with a central malonate unit. *Liq. Cryst.* **2018**, *45*, 1626–1636. [\[CrossRef\]](#)
30. Arakawa, Y.; Komatsu, K.; Tsuji, H. Twist-bend nematic liquid crystals based on thioether linkage. *New J. Chem.* **2019**, *43*, 6786–6793. [\[CrossRef\]](#)
31. Prabhu, R.; Yelamagad, C.V. Structure-property correlations in cyanobiphenyl-based dimer-like mesogens. *J. Phys. Chem. B* **2015**, *119*, 11935–11952. [\[CrossRef\]](#)
32. Arakawa, Y.; Kang, S.; Nakajima, S.; Sakajiri, K.; Cho, Y.; Kawauchi, S.; Watanabe, J.; Konishi, G.-I. Diphenyltriacylenes: Novel nematic liquid crystal materials and analysis of their nematic phase-transition and birefringence behaviours. *J. Mater. Chem. C* **2013**, *1*, 8094–8102. [\[CrossRef\]](#)
33. An, P.; Shi, Z.-F.; Dou, W.; Cao, X.-P.; Zhang, H.-L. Synthesis of 1,4-bis[2,2-bis(4-alkoxyphenyl)vinyl]benzenes and side chain modulation of their solid-state emission. *Org. Lett.* **2009**, *12*, 4364–4367. [\[CrossRef\]](#)
34. Krause, M.; Ligneau, X.; Stark, H.; Garbarg, M.; Schwartz, J.-C.; Schunack, W. 4-Alkynylphenyl imidazolylpropyl ethers as selective histamine H₃-receptor antagonists with high oral central nervous system activity. *J. Med. Chem.* **1998**, *41*, 4171–4176. [\[PubMed\]](#)
35. Smeyanov, A.; Schmidt, A. K₃PO₄-KOH Mixture as efficient reagent for the deprotection of 4-aryl-2-methyl-3-butyn-2-ols to terminal acetylenes. *Synth. Commun.* **2013**, *43*, 2809–2816. [\[CrossRef\]](#)
36. Sheldrick, G.M. Crystal structure refinement with SHELXL. *Acta Cryst.* **2015**, *C71*, 3–8.
37. Frisch, M.J.; Trucks, G.W.; Schlegel, H.B.; Scuseria, G.E.; Robb, M.A.; Cheeseman, J.R.; Scalmani, G.; Barone, V.; Petersson, G.A.; Nakatsuji, H.; et al. *Gaussian 16, Revision B.01*; Gaussian, Inc.: Wallingford, CT, USA, 2016.
38. Yanai, T.; Tew, D.P.; Handy, N.C. A new hybrid exchange–correlation functional using the Coulomb-attenuating method (CAM-B3LYP). *Chem. Phys. Lett.* **2004**, *393*, 51–57. [\[CrossRef\]](#)
39. Okuno, K.; Shigeta, Y.; Kishi, R.; Nakano, M. Non-empirical tuning of CAM-B3LYP functional in time-dependent density functional theory for excitation energies of diarylethene derivatives. *Chem. Phys. Lett.* **2013**, *585*, 201–206. [\[CrossRef\]](#)
40. Andzelm, J.; Kölmel, C.; Klamt, A. Incorporation of solvent effects into density functional calculations of molecular energies and geometries. *J. Chem. Phys.* **1995**, *103*, 9312–9320. [\[CrossRef\]](#)
41. Barone, V.; Cossi, M. Quantum calculation of molecular energies and energy gradients in solution by a conductor solvent model. *J. Phys. Chem. A* **1998**, *102*, 1995–2001. [\[CrossRef\]](#)
42. Cossi, M.; Rega, N.; Scalmani, G.; Barone, V. Energies, structures, and electronic properties of molecules in solution with the C-PCM solvation model. *J. Comput. Chem.* **2003**, *24*, 669–681. [\[CrossRef\]](#) [\[PubMed\]](#)
43. Gao, M.; Lam, J.W.Y.; Li, J.; Chan, C.Y.K.; Chen, Y.; Zhao, N.; Han, T.; Tang, B.Z. Stoichiometric imbalance-promoted synthesis of polymers containing highly substituted naphthalenes: Rhodium-catalyzed oxidative polycoupling of arylboronic acids and internal diynes. *Polym. Chem.* **2013**, *4*, 1372–1380. [\[CrossRef\]](#)
44. Bondi, A. van der Waals volumes and radii. *J. Phys. Chem.* **1964**, *68*, 441–451. [\[CrossRef\]](#)
45. Mondal, S.; Chatterjee, S.; Halder, R.; Jana, B.; Singh, C. Role of dispersive fluorophilic interaction in the solvation dynamics of the perfluoro group containing molecules. *J. Phys. Chem. B* **2017**, *121*, 7681–7688. [\[CrossRef\]](#) [\[PubMed\]](#)

46. Kuwabara, J.; Yamaguchi, K.; Yamawaki, K.; Yasuda, T.; Nishimura, Y.; Kanbara, T. Modulation of the emission mode of a Pt(II) complex via intermolecular interactions. *Inorg. Chem.* **2017**, *56*, 8726–8729. [[CrossRef](#)] [[PubMed](#)]
47. Pati, A.K.; Gharpure, S.J.; Mishra, A.K. White light emission in butadiyne bridged pyrene-phenyl hybrid fluorophore: Understanding the photophysical importance of diyne spacer and utilizing the excited-state photophysics for vapor detection. *J. Phys. Chem. A* **2016**, *120*, 5838–5847. [[CrossRef](#)] [[PubMed](#)]



© 2020 by the authors. Licensee MDPI, Basel, Switzerland. This article is an open access article distributed under the terms and conditions of the Creative Commons Attribution (CC BY) license (<http://creativecommons.org/licenses/by/4.0/>).